M. Chandnani[1,2] and R. R. Herrick[2]

[1]Nurture.farm, Bengaluru, Karnataka, India.

[2]Geophysical Institute, University of Alaska Fairbanks, Fairbanks, Alaska, USA.

Corresponding author: Robert Herrick (rrherrick@alaska.edu)

Key Points:

- In the lunar simple-to-complex transition, some highlands craters have floor slump deposits but others do not despite similar settings.
- Impacts on pre-existing slopes drove localized slumping along the direction of the slopes.
- Simple craters were formed on surfaces with topographic breaks that slope in opposite direction to the slope of adjoining crater walls.

Abstract

The 15-20 km crater diameter range on the Moon spans simple to transitional to complex crater morphologies. Simple craters in this range are only in the highlands. Transitional craters that contain localized slumps are scattered across the lunar surface. Most craters with localized slumps in the highlands superpose pre-impact topography with obvious slope breaks. We interpret this as a condition favorable for post-excavation internal slumping. However, some of these craters formed on terrains with topographic variation similar to the settings of simple craters: flat or gradually sloping surface, or degraded structures of older craters such as rims and terraces. To resolve the conundrum of two morphologies on one terrain type, we performed investigations of the local geology and topography of the inferred pre-impact terrains. We assessed if the localized slumping in the craters happened during or well after crater formation, looked for spatial variations in the strength of the highlands crust, detected topographic breaks (through elevation data) that were unnoticeable in the optical data, and examined rim circularity. Our findings corroborate the influence of pre-existing slopes on mass wasting along crater walls. The majority of the craters with localized slumps have walls superposing topographic breaks that slope towards the crater interior. These walls are located near the uphill sector of the rims which initiated localized slumping. Most simple craters were found to have formed on surfaces with topographic breaks/slopes that face away from the adjoining crater walls, so that any immediate mass wasting would likely be outside the crater cavity.

Plain Language Summary

We observed a set of lunar impact craters that are similar in size and located in similar-appearing geologic settings but have different appearances. In some of the craters there are mounds on the floor that appear to have resulted from material slumping from the crater rim. Our analysis indicates that the slumping likely occurred during crater formation, and we saw no evidence that variability

in the makeup of the lunar near-surface was a determining factor. Careful examination of the local topography suggests that slumping becomes more likely if a portion of the impacted surface slopes towards the impact point, even for modestly sloping or undulating terrain.

1 Introduction

1.1 Wall Slumping

The size-dependent simple-to-complex morphologic progression in impact craters on the Moon has been studied for over 40 years (Melosh, 1989; Pike, 1977, 1980a, 1980b). After formation of a transient parabolic cavity, crater features developed in the modification stage form the basis of a "simple" or "complex" crater morphology. For smaller craters, the walls undergo gravity-induced collapse and material slumps off the walls, thereby forming a breccia lens on the crater floor and giving the final crater a roughly parabolic profile (Melosh, 1989; Melosh & Ivanov, 1999). For lunar crater sizes greater than ~15 km (Croft, 1985; Krüger et al., 2018; Melosh & Ivanov, 1999; Pike, 1977, 1980a, 1980b, 1988), in addition to unconsolidated material from wall slumping, the onset of floor features such as terraces (sliding of discrete blocks along normal faults) and central peaks occurs, which are the diagnostic features of a complex crater morphology (Kenkmann et al., 2012; Melosh, 1989; Pike, 1980a, 1980b; Quaide et al., 1965). While complex craters on the Moon begin to form at sizes greater than ~15 km, the simple-to-complex transition occurs over a diameter range. The transition zone constitutes simple, complex and transitional craters. Transitional craters have floors that are broader than that of simple craters, contain localized or spread out unconsolidated slumped material and/or terraces while lacking a well-defined central peak (Cintala et al., 1977; Cintala & Grieve, 1998; Howard, 1974; Kalynn et al., 2013; Pike, 1974; Plescia, 2015; Robbins & Hynek, 2012; Smith & Sanchez, 1973). Chandnani et al. (2019) identified slumped debris based on gradual decrease in wall slope at the contact of the debris and wall, and terraces on the basis of a step-like pattern in topographic profiles.

Regardless of the morphology, transient cavity collapse is driven by gravity and extreme strength degradation of impacted target rocks (Melosh, 1977, 1989; Quaide et al., 1965). For the transient cavity to weaken and rock to mobilize, the effective strength of the impacted rocks has been determined to be much lower than the cohesion of intact rocks (Güldemeister et al., 2015; Kenkmann et al., 2012; Melosh, 1977, 1989), and the effective coefficient of friction is much lower than that of typical granular targets (McKinnon, 1978).

While the mechanisms driving the transient strength degradation of target rocks are still debated, several target properties can assist in lowering of rock strength. Target heterogeneities such as interlayering of different lithologies or unconsolidated sediments with cohesive substrate can create strength variations in the target and trigger cavity collapse, thereby forming slump features and/or terraces and/or central peaks. This may be why a smaller diameter has been

observed for the onset of transitional and complex craters in layered targets (Chandnani et al., 2019; Cintala et al., 1977; Cooper, 1977; Dence, 1972; Osinski et al., 2018; Pike, 1980a; Quaide & Oberbeck, 1968; Roddy, 1977; Senft & Stewart, 2008; Smith & Hartnell, 1978; Stewart & Valiant, 2006). Impact on a target characterized by spatial variations in strength can also lead to cavity collapse features. Several experimental (Aschauer & Kenkmann, 2017) and observational studies on impact craters on slopes on the Moon (Plescia, 2012; Plescia et al., 2019), and asteroids Vesta (Krohn et al., 2014) and Lutetia (Elbeshausen et al., 2012), have reported that when a hypervelocity impactor hits a sloping surface, the transient cavity grows in a direction perpendicular to the slope of the surface. The cavity wall in the uphill sector of the rim (the wall sloping in the direction of the surface slope) can get over-steepened, which initiates slumping in the form of landslides even for surface slope angles as low as 5° from horizontal. With increasing slope angles, the deepest point of the crater shifts downhill from crater-center and the depth-diameter ratio (d/D) decreases due to the mass movements. The crater shape also loses its symmetry and elongates in the downhill direction. If slope angles approach the angle of repose of the target material, the landslides can overshoot the downhill crater rim. However, no cases of craters with central peaks were observed in these studies. Other than the process of slumping during crater formation, seismic shaking from nearby younger impacts can trigger mass wasting along crater walls post-crater formation (Kumar et al., 2013; Schultz & Gault, 1975).

The narrow 15-20 km diameter range, which is a subset of the lunar simple-to-complex transition zone, constitutes a diverse group of morphologies spanning a variety of geologic settings. In order to elucidate the reasons behind these morphological variations, Chandnani et al. (2019) created a database of 244 well-preserved 15-20 km-sized lunar craters and characterized their morphologies based on their features in Lunar Reconnaissance Orbiter Camera (Robinson et al., 2010) Wide Angle Camera (LROC WAC) images, LROC Narrow Angle Camera (NAC) images and their LROC Lunar Orbiter Laser Altimeter (LOLA) (Smith et al., 2011) topographic profiles. The craters were not categorized as simple, transitional or complex, but classified according to the presence of crater units like slumped material, terraces, central uplifts, floor fractures and so on. Chandnani et al. (2019) created seven morphologic groups:

[1] Simple crater

[2] Crater with localized slumps

[3] Crater with localized slumps and terraces

[4] Crater with localized slumps and central uplift

[5] Crater with localized slumps, terraces and central uplift

[6] Concentric crater

[7] Floor-fractured crater

The cavities of the simple craters are characterized with uniform wall slopes and roughly parabolic profiles. The localized slumps refer to the unconsolidated slumped material that is confined to certain parts of the floor such that their position is marked by a gradual decrease in wall slope. Morphologies [2] and [3] are types of transitional craters while [4] and [5] can also be called complex craters due to the presence of a central uplift. The major morphologies that occupy the lunar highlands are the simple craters and the craters with localized slumps (see Figure 4 in Chandnani et al., 2019). On studying the geology of the terrains bearing these craters, Chandnani et al. (2019) noticed that the 117 simple craters occur on flat or gradually sloping surfaces or superpose degraded rims or terraces of pre-existing craters. The majority of the craters with localized slumps were formed on sharp topographic breaks such as well-developed rims, terraces or ejecta of older craters, and therefore the slumped debris could have resulted from oversteepening of a crater wall sloping in the direction of the topographic break (Aschauer & Kenkmann, 2017; Elbeshausen et al., 2012; Krohn et al., 2014; Plescia, 2012; Plescia et al., 2019). However, the topographic variation of the terrains comprising 35 of the 97 craters with localized slumps was observed to be similar (no sharp topographic breaks) to that of the terrains bearing the simple craters. Chandnani et al. (2019) also noted that the depth ranges of the simple craters and craters with localized slumps show a significant overlap. A preliminary examination

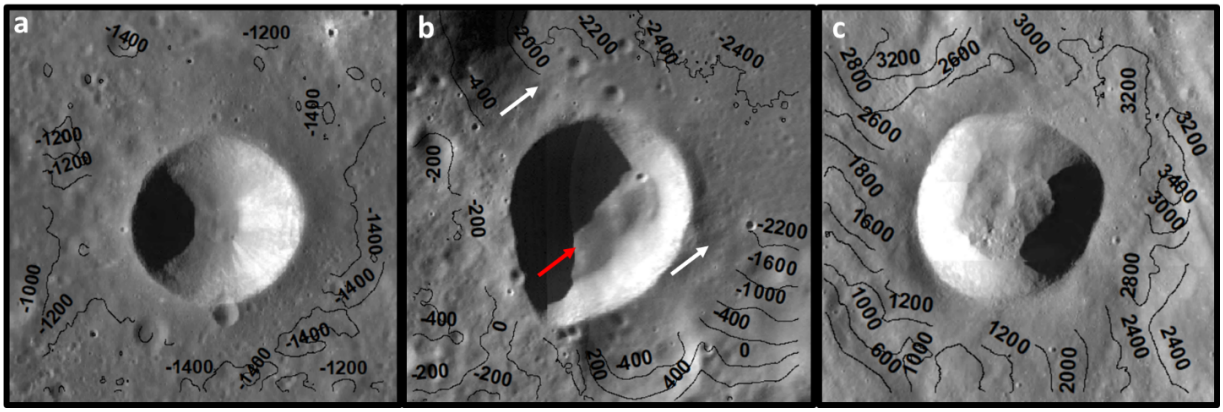

Figure 1. LOLA elevation contours superposed on WAC images of 15-20 km-sized simple craters and craters with localized slumps on highlands terrains. a) Simple crater Isidorus D (-4.27°N, 34.07°E) located on a flat highlands surface; b) Crater Unnamed2 (-56.32°N, 90.33°E) with localized slumps that superposes the terrace of a pre-existing larger crater; c) Crater Leuschner Z (5.24°N, 250.43°E) with localized slumps located on a highlands terrain that gradually slopes from north to south. The contours represent the pre-impact terrain elevation acquired from LOLA DEMs and begin at 1.5 radii from the crater center to avoid the ejecta. The elevation values are in meters. In (b) the terrace is the slope on which the crater was formed. The red arrow in (b) refers to the wall that slopes in

the direction of the terrace slope (white arrows) and therefore experienced mass wasting from oversteepening, which is also evidenced by the uphill extension of that part of the rim. All images are 30 km wide. North is up in all images.

of the geology of the two terrains indicated that no other differences in the target properties were visible that could justify the presence of localized slumps in the 35 craters and their absence in the simple craters. Figure 1 shows examples of the kind of topographic trends followed by pre-impact terrains of simple craters and craters with localized slumps. The elevation contours highlight the topographic variations.

1.2 Objective

We seek to determine the factors responsible for whether slumping occurs, and where it occurs, in 15-20 km-sized craters on target terrains that appear flat or gently undulating in LOLA-derived topography. We propose and investigate three working hypotheses:

[1] *Localized slumping occurred post-crater formation:*

It is possible that the 35 craters with localized slumps formed with simple crater morphologies, and slumping occurs later due to seismic shaking caused by nearby younger impacts (Kumar et al., 2013; Schultz & Gault, 1975).

[2] *Localized slumping occurred on a weaker target:*

As described earlier, wall collapse is caused by target strength degradation and gravitational force (Güldemeister et al., 2015; Kenkmann et al., 2012; Melosh, 1977, 1989; Quaide et al., 1965). The greater the strength, the less intense is the collapse. The highlands crust has been battered by impacts since its formation. The shock waves from these impacts have resulted in fractured and fragmented crust in the form of crater ejecta (Heiken et al., 1991), crater modification features, ~10 km-deep fractured bed rock called megaregolith (Hartmann, 1973) and meters thick fine-grained surface regolith (Bart et al., 2011; Papike et al., 1982). Continuous impacts and fragmentation could have led to spatial heterogeneties in the highlands crustal strength, Therefore, we hypothesize that localized slumping occurred on the highlands terrains whose strength is lower than that of the terrains that bear simple craters in the same size regime.

[3] *Impact cratering on a slope causes the localized slumping:*

For 62 highlands craters in our initial study set that have localized slumps, it was clear that the crater formed on pre-impact terrain that had a significant topographic break. The localized wall slumping was predominantly on the uphill rim sector due to impact cratering on slopes (Aschauer & Kenkmann, 2017; Elbeshausen et al., 2012; Krohn et al., 2014; Plescia, 2012; Plescia et al., 2019). Similarly, there may have been subtle topographic heterogeneities in the pre-impact terrains of the 35 craters with localized slumps that have been obscured by younger impact craters and their ejecta and therefore are not obvious in the LROC WAC and NAC images. These heterogeneities may have served as slopes

for the transient cavity walls that were superposing them and sloping in the same direction, and caused them to oversteepen and collapse, thereby resulting in localized slumped material.

2 Methods and Data

2.1 Hypothesis 1 test: Comparison of crater counts on slump units with ejecta units of craters with localized slumps

If the localized slumped material accumulated post-crater formation, it is younger than the crater's ejecta. On airless bodies like the moon, new surfaces immediately begin collecting craters. An older surface would contain more craters per unit area than a younger surface, all else being equal. Counting of craters above a specified size on a given surface gives a crater size-frequency distribution (CSFD). Combined with an estimate of the rate of production of craters, the CSFD can be use to estimate the age of a surface (Neukum et al., 1975a; Neukum et al., 1975b; Neukum, 1983). For each of the 35 craters with localized slumps, we used 512 ppd LOLA DEMs to delineate regions of the slumped material and ejecta that are nearly flat (slope angles of 0°-7°) to discard the influence of surface relief on a CSFD. The slumped material is positioned along the crater wall and can therefore have less flat and more steep surfaces. Craters whose slumped material did not have flat surfaces were excluded from the crater counting analysis. The area of ejecta beyond 1.25 crater radii (R) from the crater center showed up as nearly flat. So, we created an annulus from 1.25 R to 1.5 R for the crater counts on the ejecta surface. The upper limit of 1.5 R was selected because the ejecta profile starts levelling out at this distance and begins transitioning into the pre-impact terrain topography. Figure 2 illustrates the selected flat regions of the two units in a crater with localized slumps. Next, we used 10 m/pixel Kaguya Terrain Camera (TC) images (Haruyama et al., 2008) to outline rims of craters on the delineated regions of the slumps and ejecta of each crater starting at 100 m diameter. A Kaguya TC image provides views of the lunar surface at moderate sun angles that allow for easier detection of surface features, and larger coverage (width of ~50 km) as compared to the higher resolution NAC image data, which minimizes sun-angle variation across the area of coverage. On fitting circular outlines to the crater rims with the help of the CraterTools in ArcGIS (Kneissl et al., 2010), we obtained their diameters as well. For each crater belonging to the group of 35 craters, the cumulative crater densities (N) corresponding to the localized slumps and ejecta units were obtained by dividing the number of craters (with diameters up to a value) belonging to each unit by the area of the unit. The cumulative crater densities were used to generate separate log-log CSFD plots for the slumps and ejecta of each crater. The crater diameters were binned at 18 equally spaced intervals per 10 km, which is called pseudo-log binning (Neukum, 1983). The error bars on each data point were calculated by dividing the square root of the respective cumulative frequency by the surface area of the unit (Arvidson et al., 1979). Using the Craterstats program developed by Michael and Neukum (2010), we

fit crater production functions updated by Neukum et al. (2001) to each CSFD. A production function is a polynomial curve that provides an estimate of the number and size of craters expected on a surface of a given age, and curves for different surface ages can be compared to a CSFD to provide an estimate of the cumulative crater density at diameter (D) of 1 km (N(1)) for that CSFD (Neukum, 1983; Neukum & Ivanov, 1994; Neukum et al., 2001). The values of N(1) has been inferred to be a measure of the age of the respective surface unit (Neukum, 1983; Neukum & Ivanov, 1994; Neukum et al., 2001). Therefore, if the N(1) values corresponding to the slump and ejecta units fall within each other's error bars (square root of cumulative crater frequency at D of 1 km divided by surface area of the unit), it means that localized slumping likely occurred around the time of ejecta deposition, that is syn-crater formation. If the N(1) values fall outside the error bars, the slumped material accumulated post-crater formation and therefore it is possible that such craters were initially formed as simple craters. The CSFD bins along or parallel to the Hartmann (1984) saturation line were excluded from the production function fit because crater densities along this line imply that the number of craters created is equal to the number of craters destroyed. This applied to parallel bins as well because craters belonging to these bins may not reach the crater density that would coincide with the saturation line because of faster obliteration on rough highlands terrains, but have the same characteristics as bins along the saturation line. Chandnani et al. (2019) (see Figure S4 of that paper) performed crater counting on a few craters with localized slumps and found that crater densities on ejecta and slump units of one of the three craters statistically differed from each other. This preliminary result is our motivation to expand the crater counting task to the 35 craters with localized slumps and eliminate the deduced simple craters from the list.

Crater degradation through time involves certain changes in the crater geometry. A widely accepted model that explains the evolution of crater topography through time is the topographic diffusion model (Bouley & Baratoux, 2011; Craddock & Howard, 2000; Fassett & Thomson, 2014; Kreslavsky et al., 2013). According to this model, rim and wall collapse and consequent slumping can continue post-crater formation primarily due to seismic shaking from late impacts (Kumar et al., 2013; Schultz & Gault, 1975), which results in progressive lowering of rim height, reduction in wall slopes and shallowing and broadening of the crater floor. Topographic profiles of the craters inferred as simple from the crater counting procedure were compared with the profiles of inferred craters with localized slumps to verify the accumulation of slumped material in the simple craters as a result of crater degradation through topographic diffusion.

2.2 Hypothesis 2 test: Frequencies of proximal simple craters and craters with localized slumps

If there are regional spatial variations in the strength of the highlands crust, then a greater number of simple craters should be formed in the stronger geologic settings whereas the weaker terrains should contain more craters with localized

slumps. Therefore, using LROC WAC images, we looked for and counted simple craters and craters with localized slumps in the simple-to-complex transition zone starting at a D of 15 km within a radius of 100 km from the center of all 117 simple craters and the 35 craters with localized slumps. We extended the crater diameter range for the proximity craters to beyond 20 km and set the upper limit to 40 km because recent studies have found transitional craters that measure up to ~40 km in size (Osinski et al., 2018). Only those craters were included that occur on flat surfaces, gradually sloping surfaces or superpose degraded craters, that is, the type of terrains on which the 15-20 km-sized simple craters and 35 craters with localized slumps were formed. Maps of the relative percentages of the proximal craters with localized slumps with respect to the percentages of the proximal simple craters were generated for each 15-20 km-sized crater. The maps would indicate if the 35 craters with localized slumps are surrounded by most craters with the same type of morphology (and hence weaker terrains) or if there are clusters of higher percentages of simple craters or craters with localized slumps in particular geologic settings surrounding both crater morphologies.

2.3 Hypothesis 3 test: Topographic variation in pre-impact terrains of the simple craters and craters with localized slumps along with rim circularity

The region located between a distance of 1.5 R (where the ejecta profile levels out) and 2 R from crater center was selected for the study of pre-impact terrain topography. For all 117 simple craters and 35 craters with localized slumps, with the help of LOLA DEMs, we created aspect-slope maps of the pre-impact region that would indicate if there are slopes reflecting breaks in elevation that went unnoticed in the optical images and simultaneously display the aspect (slope direction) associated with each slope value. All aspect values were measured as azimuthal directions, that is, clockwise from North (0°). Similar maps were generated for the crater interior whose circular boundary was set at a distance of 1 R from the crater center. Presence of pre-impact terrain slope whose aspect is similar to adjoining crater walls would reflect the possibility of impact cratering on slopes.

The rim of a simple crater is roughly circular in outline, but the rim outline of a transitional or a complex crater has been observed to show deviations from circularity because of more intense and non-uniform collapse of different sectors of the rim and crater wall (Pike, 1977, 1980b; Pike, 1981). Localized slumping will also lead to an asymmetric crater shape and a non-circular rim outline. We used the Polsby-Popper Score (PP) (Cox, 1927) to determine the degree of circularity of the rims of the simple craters and craters with localized slumps. The formula for PP is

(1) $PP = 4\ A/p^2$,

where A = Area of the polygon encompassing the crater interior and whose boundary is the rim outline, and p = perimeter of the polygon encompassing the crater interior and whose boundary is the rim outline. PP always ranges

from 0 to 1. A value of 0 refers to a completely non-circular rim (an infinite perimeter) and 1 means a perfectly circular rim. For craters on flat surfaces with/without layering, terrains with topographic breaks whose sloping directions are opposite to that of adjoining crater walls with/without layering and terrains with breaks that slope in the same direction as the superposing crater walls with/without layering, box plots of *PP* scores were generated to obtain the ranges and the distribution of the score values that would indicate how different types of heterogeneities in the crust have contributed to the final crater morphology. A scatter plot of *PP* scores against crater floor diameters for simple craters was also constructed with the same terrain classification that was used for the box plots. This is because minor localized slumping, though not visible in the profiles of simple craters, can aid in broadening of the crater floor (Bouley & Baratoux, 2011; Craddock & Howard, 2000; Fassett & Thomson, 2014; Kreslavsky et al., 2013), causing deviation from rim circularity and hence a reduction in the *PP* score. So, the scatter plot would signal if the variations in the *PP* scores with spatial variations in topography, or layering is a consequence of variations in slumping. The floor diameters measured for the morphometry plots in Section 2.3.3 of Chapter 2 were used in this study.

3 Results

3.1 Comparison of crater densities on slumps and ejecta units of craters with localized slumps

Only 20 of the 35 craters with localized slumps were selected for the crater counting task because we did not find flat areas (slope angles in the range 0°-7°) on the surfaces of the localized slumped material in 13 craters and the Kaguya TC images of two craters located beyond latitudes of 50° (Poincare C at -54.59°N, 168.7°E and Schwarzschild Q at 66.24°N, 108.83°E) appeared to be partially shadowed. Of the 20 craters, 5 craters could possibly be simple craters in which material slumped locally post crater formation because the N(1) corresponding to the ejecta units was statistically different and greater than that of the slump

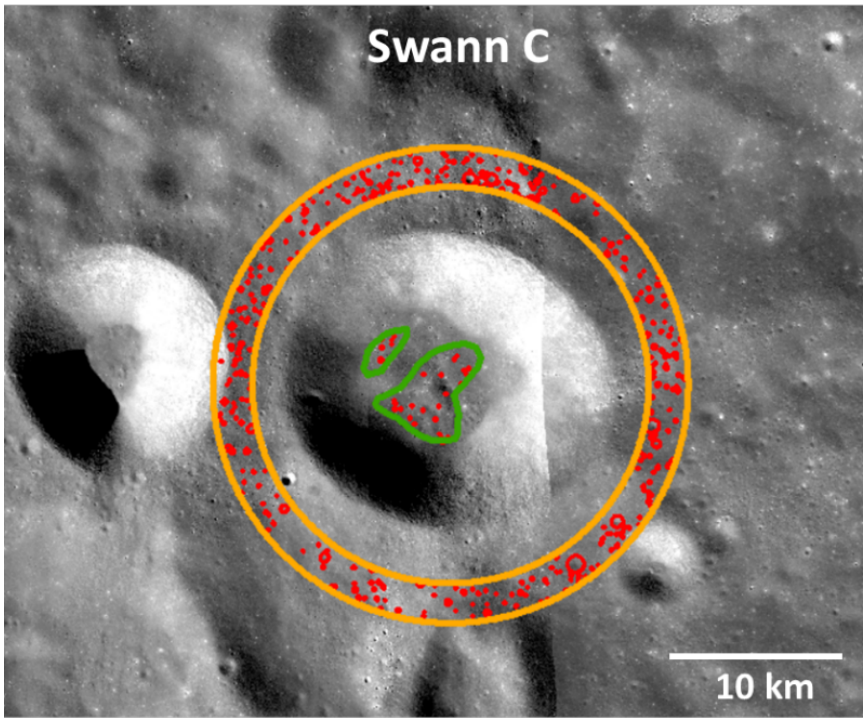

Figure 2. Slump and ejecta units mapped on the Kaguya TC image of crater Swann C that has localized slumped material. It is located at 52.9°N, 114.28°E. The annulus outlined in orange refers to the ejecta unit and the area outlined in green is the area of the localized slumps selected for crater counting based on flat suface criteria (slope angles of 0°-7°). The craters detected in both units are marked with red circular outlines. North is up.

units. In case of the remaining 15 craters, the N(1)s of the ejecta and slump units were observed to be statistically similar which suggests that they formed as craters with localized slumps. In Figure 3, log-log CSFD plots and their production function fits for the ejecta and slump units of 2 of the 5 inferred simple craters and 2 of the 15 inferred craters with localized slumps have been displayed. The remaining plots are available in Figure S1 of the Supplemental Material. The N(1) values with their error bar values are listed in Table 1 and in the legends of Figure 3 and Figure S1.

Figure 4 shows the topographic profiles of the four craters discussed in Figure 3. The elevation and surface distance have been normalized to the crater diameter. The crater shapes (wall slopes, rim heights) are similar except for a lowered rim in the area where the slump material appears to originate. We observed similar morphometric trends from the profiles of the remaining craters.

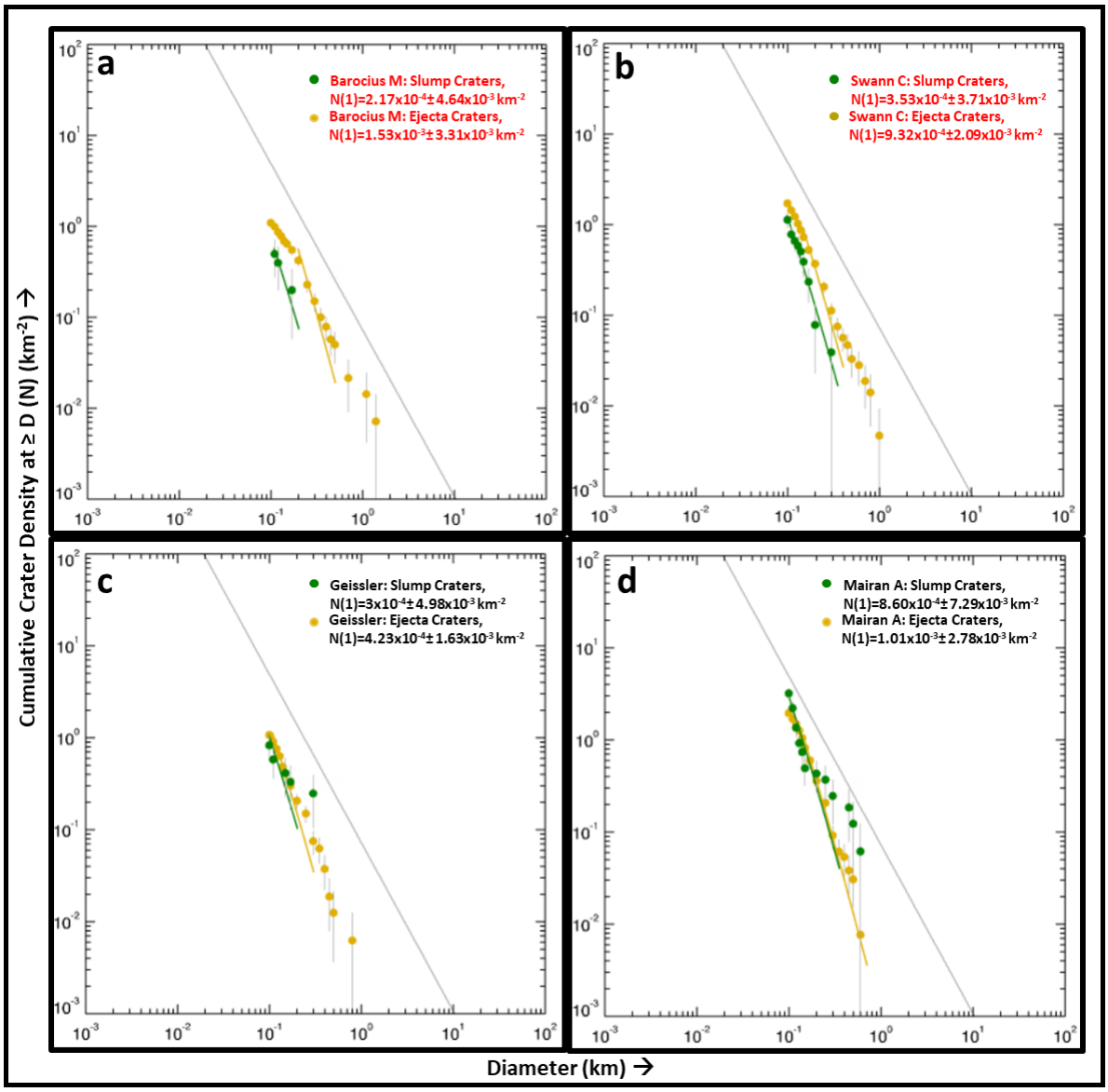

Figure 3. Log-log CSFD plots corresponding to ejecta and slump units of four craters with localized slumps. From the production function fits, a) Barocius M (-42.45°N, 19.48°E) and b) Swann C (52.9°N, 114.28°E) appear to be simple craters whose walls collapsed after crater formation (represented by N(1) values in red font) while c) Geissler (-2.59°N, 76.5°E) and d) Mairan A (38.63°N, 321.21°E) appear to have slump blocks that formed synchronously with the crater. The green and orange dots represent the crater bins of slumps and ejecta respectively. The green and orange lines are the best fit production func-

tions for the CSFDs of slump and ejecta units respectively. The grey sloping line is the Hartmann (1984) crater saturation line. The N(1) values are given in the legends on the top right area of each plot.

Table 1. List of cumulative crater densities at D of 1 km (N(1)) along with error bar values for the slump and ejecta units of the selected 20 craters with localized slumps in the 15-20 km diameter range. The rows highlighted in bold refer to the craters whose localized slumped material possibly accumulated after crater formation.

Crater Name	Latitude (°N)	Longitude (°E)	Diameter (km)	N(1) of slump unit (km^{-2})
Barocius M	**-42.45**	**19.48**	**16.09**	**$2.17x10^{-4}\pm 4.64x10^{-3}$**
Bell J	19.88	265.88	20.03	$6.16x10^{-4}\pm 4.58x10^{-3}$
Bode	6.7	357.54	18.17	$7.02x10^{-4}\pm 6.20x10^{-3}$
Coriolis S	0.1	169.66	17.7	$3.81x10^{-4}\pm 8.42x10^{-3}$
Dreyer R	**8.49**	**94.47**	**19.9**	**$4.12x10^{-4}\pm 3.40x10^{-3}$**
Fryxell	-21.25	258.34	17.57	$9.96x10^{-4}\pm 7.52x10^{-3}$
Geissler	-2.59	76.5	17.21	$3x10^{-4}\pm 4.98x10^{-3}$
Hahn A	**29.66**	**69.72**	**18.74**	**$1.99x10^{-4}\pm 6.04x10^{-3}$**
Hahn B	31.37	76.97	16.74	$8.20x10^{-4}\pm 6.48x10^{-3}$
Harkhebi T	40.04	95.31	18.4	$2.83x10^{-4}\pm 6.74x10^{-3}$
Hatanaka Q	25.99	235.34	19.05	$3.71x10^{-4}\pm 5.56x10^{-3}$
Hommel J	**-53.53**	**27.87**	**17.51**	**$2.24x10^{-4}\pm 3.18x10^{-3}$**
la Condamine A	54.43	329.8	18.25	$5.47x10^{-4}\pm 1.16x10^{-2}$
Leucippus K	27.27	244.49	15.55	$6.89x10^{-4}\pm 1.46x10^{-2}$
Mairan A	38.63	321.21	15.9	$8.60x10^{-4}\pm 7.29x10^{-3}$
Swann C	**52.9**	**114.28**	**19.87**	**$3.53x10^{-4}\pm 3.71x10^{-3}$**
Unnamed16	34.92	176.71	17.24	$8.00x10^{-4}\pm 1.05x10^{-2}$
Unnamed33	15.15	224.18	18.36	$5.22x10^{-4}\pm 5.77x10^{-3}$
Unnamed36	-44.87	225.13	16	$3.29x10^{-4}\pm 6.83x10^{-3}$
Van de Graaff C	-26.43	172.81	18.15	$4.49x10^{-4}\pm 5.60x10^{-3}$

There could be errors in the CSFDs of the five inferred simple craters stemming from inaccurate representation of the slump and ejecta units by the counted craters. This is because the crater density on the highlands is high enough that newly formed craters can overlap with or superpose older craters. So, ejecta from nearby craters may mask the craters superposing the slump and ejecta units thereby reducing the crater densities. Figure 2 illustrates the masking of a part of slumped material by a nearby crater's ejecta (north-west of Swann C). Small slumps along the crater wall throughout the crater's life in the form of dry granular flows (Kumar et al., 2013) may also fill the craters on some parts of pre-existing slump units and therefore result in lower-than-expected crater densities, so for the craters with apparently young slump blocks it may be that only a thin uppermost layer is younger.

3.2 Frequencies of proximal simple craters and craters with localized slumps

We were able to detect well-preserved proximal simple craters and transitional craters for 83 simple craters and 24 craters with localized slumps. The transitional craters included craters

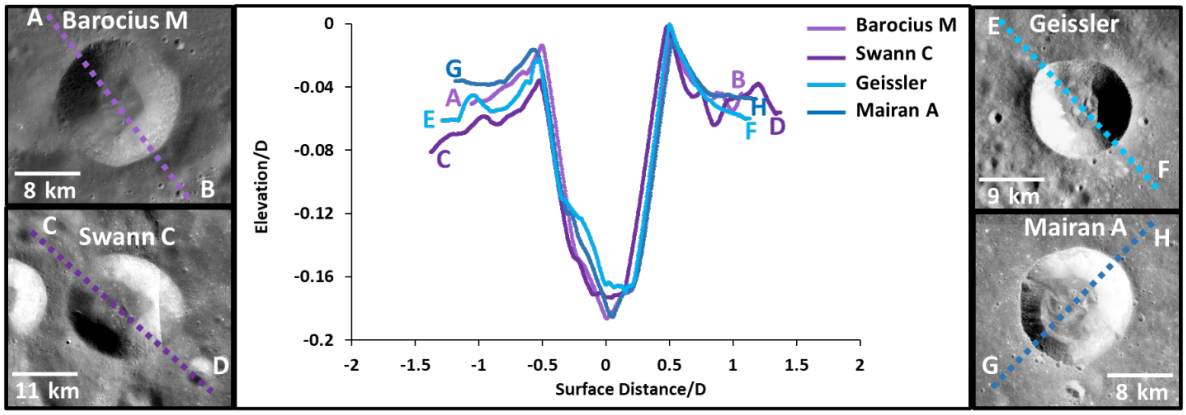

Figure 4. LOLA topographic profiles (center) of craters whose CSFD plots are shown in Figure 3. The profiles are accompanied by Kaguya TC images of craters Barocius M and Swann C (N(1)s of slump units are statistically lower than that of ejecta units) on the left and craters Geissler and Mairan A (N(1)s of slump and ejecta units are statistically similar). In the profiles, the surface distance and elevation are scaled to the respective crater diameters. North is up in all images.

with localized slumps and craters with broader, flatter floors. The flat-floored craters started appearing at diameters greater than 25 km. Each 15-20 km diameter crater was surrounded by a maximum of six well-preserved craters in the simple-to-complex transition zone. The distribution of percentages of surrounding transitional craters relative to that of simple craters have been mapped in Figure 5 for simple craters and Figure 6 for craters with localized slumps. The graduated sizes of the circles refer to the classes of the total number of proximal craters. The shades of circles represent the relative percentages where magenta shades reflect that the simple craters outnumber the transitional craters (negative values). The pre-dominant presence of purple shades (0-60%) and blue (60-100%) circles in both Figures indicates that the distributions of proximal craters skewed towards transitional crater morphology. Proximal transitional craters outnumbered proximal simple craters for 80% of the simple craters and 75% of the craters with localized slumps. In 67% of the cases for both morphologies, only proximal transitional craters were detected. The craters surrounded by higher relative percentages of proximal simple craters exist in patches across the lunar surface in both Figures. The percentages are available in Table S1 of the Supplemental Material.

3.3 Topographic variation in pre-impact terrains of the simple craters and craters with localized slumps along with rim circularity

The aspect-slope maps of crater cavities and pre-impact terrains reveal that 64% of simple craters are located on flat or gradually sloping surfaces or superpose topographic breaks that slope in a direction opposite to the adjoining crater walls and away from crater center. Around 60% of craters with localized slumps have walls that slope in the same direction as the superposed topographic breaks (which are thus towards crater center). The breaks are rims or terraces of pre-existing craters and are more noticeable in the aspect-slope maps than in the optical images. Figures 7 (simple craters) and 8 (craters with localized slumps) illustrate pre-impact terrains that are gradually sloping and have topographic breaks that are sloping in or opposite to the direction of slopes of adjoining crater walls. In cases of craters with localized slumps, we did not encounter surfaces that are completely flat, unlike the case of simple craters where 50% of surfaces are sloping at angles $< 7°$. The color wheel in the legend symbolizes the aspect values in the aspect-slope maps. The three rings of the wheel denote different classes of slopes. The saturation values of the colors reduce with decrease in slope

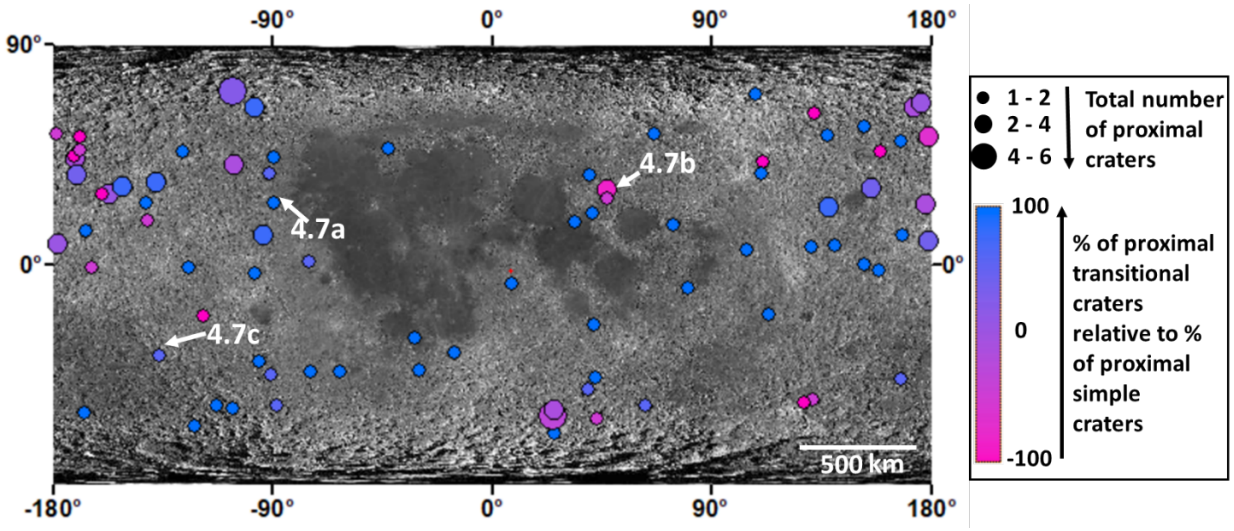

Figure 5. Mapped distribution of percentages of transitional craters relative to simple craters in the proximity of 83 15-20 km diameter simple craters. The graduated sizes of the circles are in increasing order of total number of proximal craters. The shades of the circles represent the percentages. The legend is available on the right. The LROC WAC mosaic has been used in the background. The alphanumeric labels refer to the locations of the craters displayed in Figure 7. The dominance of purple and blue shades is evident which means that most simple craters are surrounded by greater number of transitional craters. North is up.

angles. Slope values ranging from 0-7 are symbolized by grey regardless of the aspect to represent flat or gradually sloping surfaces. The relevant slopes of the walls and topographic breaks are marked by arrows. The LOLA elevation contours superposed on WAC images above the aspect-slope maps highlight the topographic variation of the pre-impact terrains. We obtained similar values of topographic break slopes for both morphologies, ranging from 8° to 15°. Details of the slopes and locations of topographic breaks are listed in Table S2 of the Supplemental Material.

Figure 9 shows the box plots of *PP* scores of simple craters (Figure 9a) and craters with localized slumps (Figure 9b) for different types of pre-impact heterogeneities. While the pre-impact terrains in case of simple craters have also been classified by presence and absence of layering, this classification has been merged with the classes by topographic variation for craters with localized slumps due to their smaller sample sizes. It can be observed that the bulk of *PP* scores in all classes of simple craters range from 0.98 to 0.995 (boxes) which indicates a nearly circular rim. The median values are also clustered around 0.99. But with the onset of layering and presence of topographic breaks sloping in similar/opposite direction to the crater walls, the bottom whiskers that could also include outliers show a drop in minimum *PP* scores to 0.95-0.96 as compared to the lower bounds of bottom whiskers in flat/gradually sloping surfaces. The bulk distributions (boxes) for craters with localized slumps exhibit a similar pattern of overlapping ranges of *PP* scores from 0.975 to 0.987 that are lower than those for simple craters. Some outlier craters also exist in case of topographic breaks that slope in the same direction as the crater walls, whose minimum *PP* scores (lower bounds of bottom whiskers) are slightly smaller (0.955) but not significantly different from the minimum scores of the 'No Break' outlier craters (0.965). The *PP* score distribution for the topographic breaks that slope in opposite directions to the crater walls display smaller ranges with the largest minimum value (0.975) and lower bounds of the box (0.985). This observation accompanies the caveat that the sample size is too small (four) to draw any inference from this result.

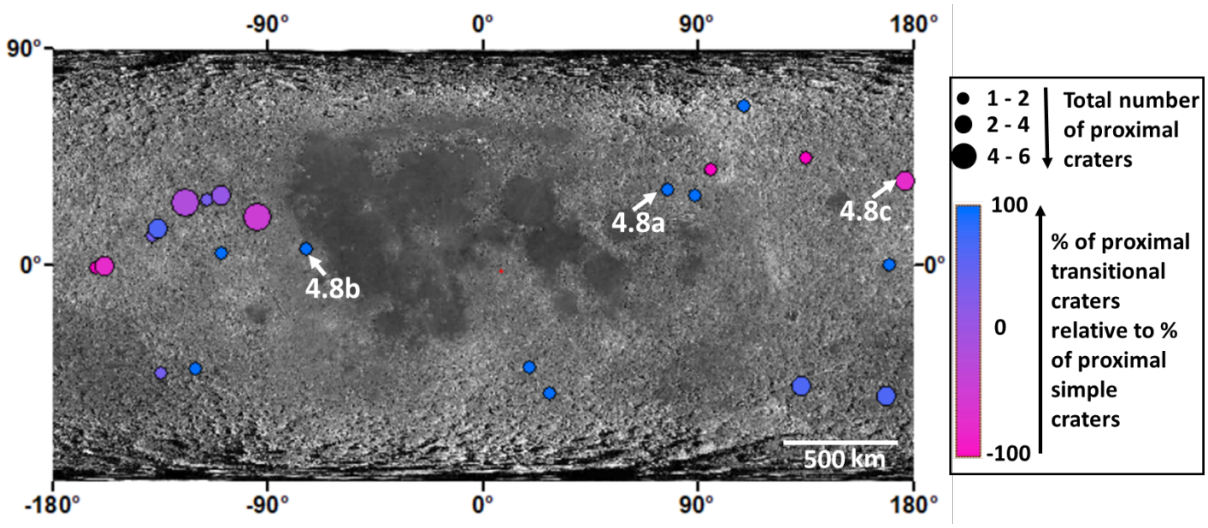

Figure 6. Mapped distribution of percentages of transitional craters relative to simple craters in the proximity of 24 15-20 km diameter craters with localized slumps. The graduated sizes of the circles are in increasing order of total number of proximal craters. The shades of the circles represent the percentages. The legend is available on the right. The LROC WAC mosaic has been used in the background. The alphanumeric labels refer to the locations of the craters displayed in Figure 8. Similar to Figure 7, the dominance of purple and blue shades, that is, the outnumbering of proximal simple craters by proximal transitional craters is evident from this Figure as well. North is up.

The scatter plots of *PP* score vs simple crater floor diameter in Figure 10 convey that most of the floor diameters are confined to a range of 0.2 to 0.4 corresponding to the *PP* score cluster between 0.98 and 0.995. For pre-impact terrains without topographic breaks, the floor diameters are exclusively restricted to the range of 0.2 – 0.4. With the onset of topographic breaks irrespective of their orientation with respect to crater walls, in addition to the clustering mentioned above, the floor diameters show an expansion in the range by an increase in the upper bounds to values as high as 0.55 similar to the shift of the lower limits of the *PP* score range to smaller values. The role of layering is not clear because the maximum values of floor diameters for all cases of terrains with topographic breaks with/without layering appear to be similar.

4 Discussion

We did not find clear evidence that any of the 35 craters with localized slumps formed as simple craters and later experienced slumping. This is because although the CSFD plots of five craters indicate simple crater morphologies, the crater profiles suggest that they formed as craters with localized slumps. Thin layers of debris from slumping post-crater formation possibly overlie the bulk of the slumped material and consequently produce errors in the CSFD plots.

So, the hypothesis stating that fresh-appearing craters with localized slumps that are located on terrains with similar topographic variation as simple craters accumulated slumped material post-crater formation is not supported by our data. We note that we are not concluding that post-impact slumping does not occur; rather, we maintain that it occurs in tandem with other degradational processes that round the rim, decrease the wall slopes, and transform the crater from "fresh" to degraded.

While looking for craters surrounding the simple craters and craters with localized slumps, we observed that transitional crater morphologies are predominant not only around the craters with localized slumps (75% of the cases) but also around simple craters (80% of the cases). In short, if strength variations in the highlands are responsible for the presence or absence of internal slumping, then the spatial scale of that variation must be smaller than the 200 km diameter circle that we used for our testing.

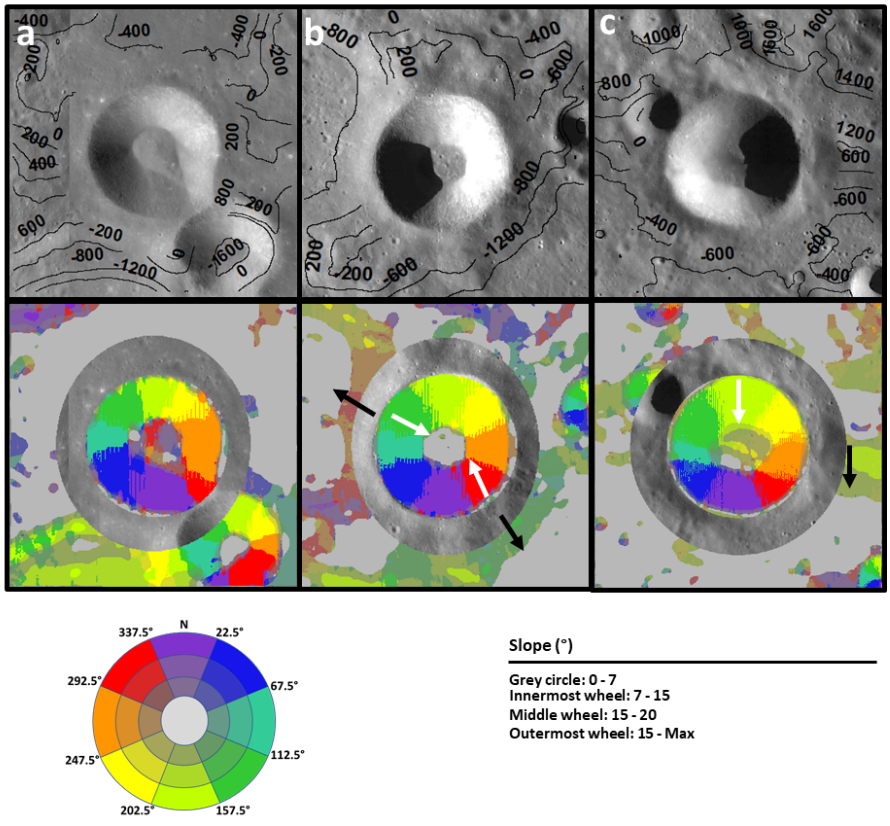

Figure 7. LOLA elevation contours (meters) superposed over WAC images of simple craters (top) and aspect-slope maps of their pre-impact terrains and crater cavities (bottom). The color wheel in the legend explains the aspect

values oriented clockwise from North. The circle and the rings represent different classes of slopes that are shown on the right of the legend. a) Crater Bartels A (25.69°N, 270.3°E) on a gradually sloping surface (S-N). The crater on its south-east formed later, so it's not counted as a topographic break. b) Crater Geminus D (30.57°N, 47.29°E) superposing rims of older craters whose walls lsope in opoosite direction theat of its walls. The grey region around the older craters shows that their ejecta are too degraded to be counted as topographic breaks. c) Crater Unnamed32 (-36.9°N, 223.5°E) whose crater wall superposes a part of an outer wall of an older crater that slopes in the same direction as the wall. The smaller crater on the north-west is not counted because it formed later than Unnamed32. All images are 33 km wide. North is up in all images.

Our third hypothesis, that the slope and orientation of pre-impact topography influences whether or not slumping occurs, is best supported by our data.

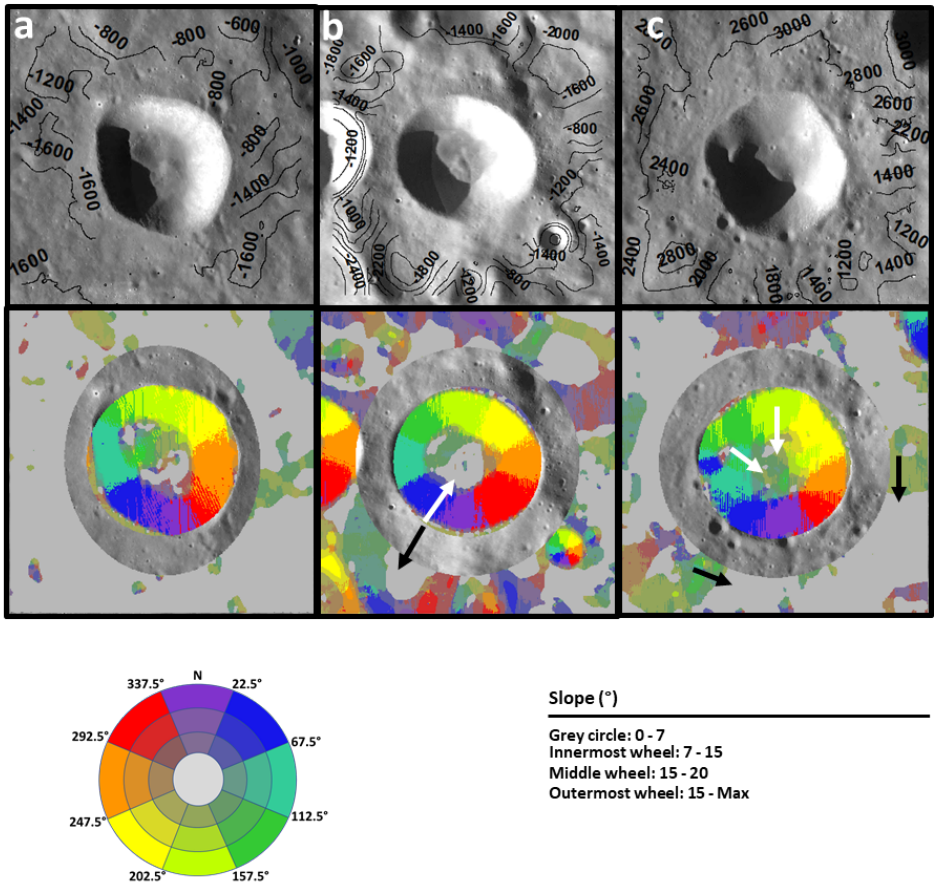

Figure 8. LOLA elevation contours (meters) superposed over WAC images of craters with localized slumps (top) and aspect-slope maps of their pre-impact

terrains and crater cavities (bottom). The color wheel in the legend explains the aspect values oriented clockwise from North. The circle and the rings represent different classes of slopes that are shown on the right of the legend. a) Crater Hahn B (31.37°N, 76.97°E) on a gradually sloping surface (NE-SW). b) Crater Swann C (52.9°N, 114.28°E) superposing the rim of an older crater whose walls slope in opoosite direction to that of its walls. The remaining topographic breaks around it can be ignored because they do not adjoin the walls. c) Crater Unnamed16 (34.92°N, 176.7°E) whose crater walls superpose the inner walls of a larger, older crater that slope in the same direction as Unnamed16's walls. The localized slumps are also positioned along these inner walls. All images are 33 km wide. North is up in all images.

The detection of topographic breaks sloping in a similar direction as the superposed crater wall for 60% of the craters with localized slumps and breaks sloping in the opposite direction to the adjoining wall for 64% of the simple craters supports this hypothesis. For an impact where a portion of the pre-existing topography slopes towards crater center, the cavity wall near the uphill rim sector is likely to get oversteepened and consequently collapse. (Aschauer & Kenkmann, 2017; Elbeshausen et al., 2012; Krohn et al., 2014; Plescia, 2012; Plescia et al., 2019). If a portion of the pre-existing topography slopes away from crater center, the outcome is a portion of the rim that is lower and perhaps outward from crater center. The formation of transient cavity and the resulting orientations of its walls on a slope is demonstrated in Figure 11. In Figure 12, the 3D illustrations of simple craters on breaks sloping away from the walls and craters with localized slumps on slopes facing the walls help in interpreting the observed association of the two crater morphologies with the two types of topographic variations in pre-impact terrains. We also found that the terrains associated with the 10 craters with localized slumps that were devoid

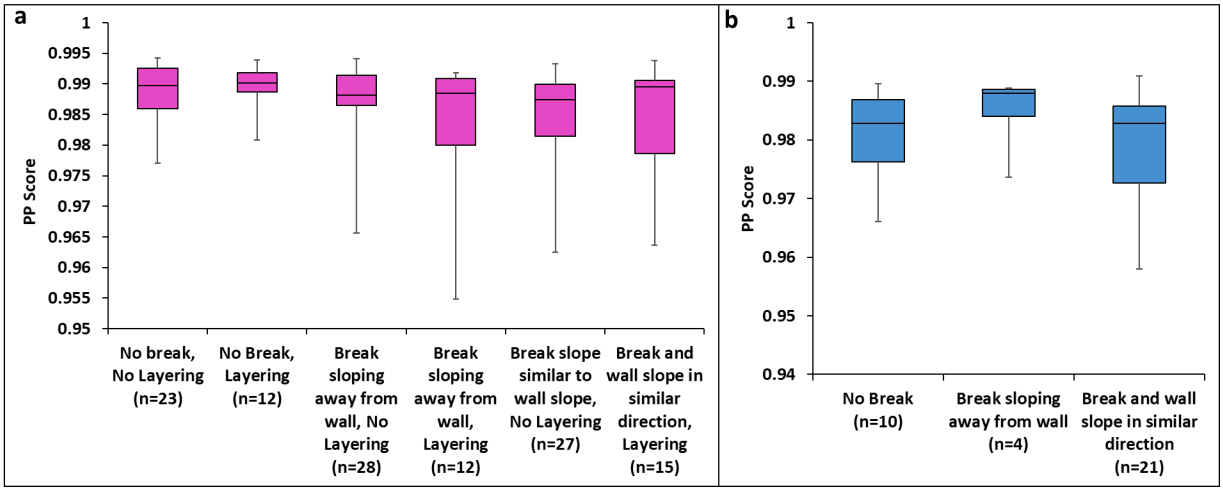

Figure 9. Box plots of *PP* scores of a) simple craters and b) craters with local-

ized slumps. The distributions have been classified by the types of topographic heterogeneities in the pre-impact terrains. The classifications have been subdivided by presence/absence of layering in case of simple craters. The letter 'n' in parentheses below the x-axis labels refers to the sample sizes associated with the types of heterogeneities.

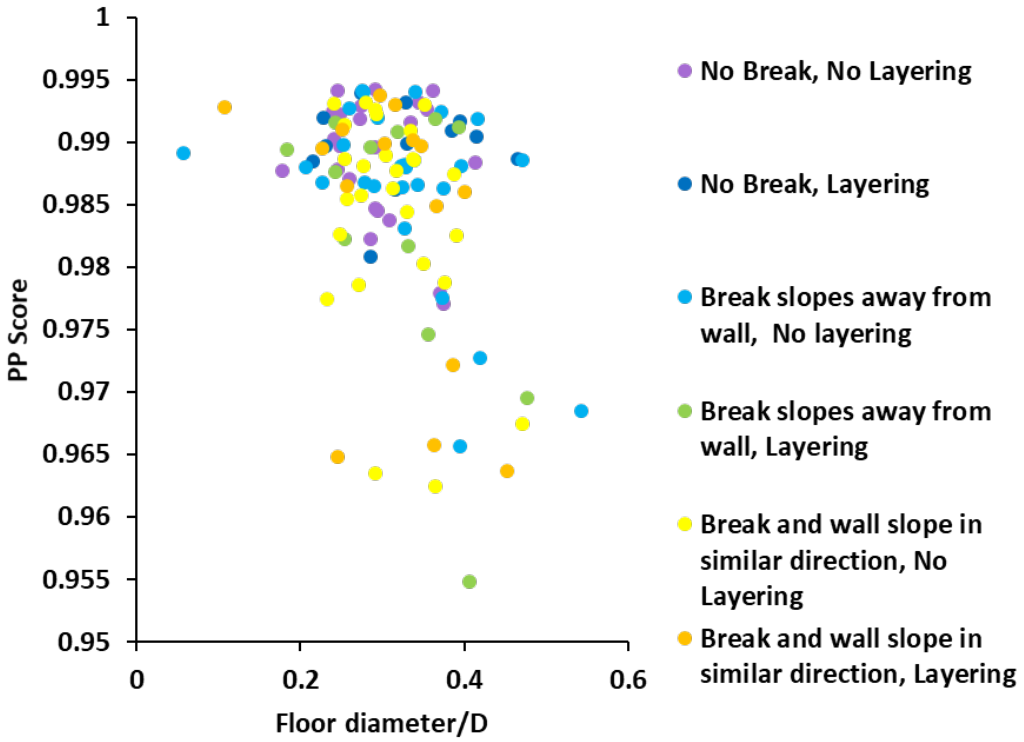

Figure 10. Scatter plots of *PP* score vs simple crater floor diameter scaled to crater diameter for various topographic heterogeneities and presence/absence of layering in the pre-impact terrains. The colors symbolize the heterogeneities.

of topographic breaks were not flat but characterized with minor slopes with maximum values of 7°. Aschauer and Kenkmann (2017) reported that mass wasting along walls can occur for slope angles as low as 5°, and therefore these minor slopes could have triggered the localized slumping as well. The broader ranges of the *PP* scores due to smaller values of lower bounds for both crater morphologies on terrains containing topographic breaks suggests that the presence of a slope caused the decrease in symmetry of the crater rim and hence the existence of lower *PP* scores. The mass wasting along the wall in the uphill sector of the rim results in the asymmetry of the rim. For topographic breaks sloping away from crater walls, the mass wasting is initiated outside the downhill sector rim from the emplacement of ejecta along the slope of the topographic

break which also causes deviations from rim circularity. The high values of *PP* scores and low values of floor diameters in the majority of simple craters is understandable because minor slumping (as compared to more intense localized slumping) during crater formation is less likely to change the shape of the rim or the floor size. However, on terrains with topographic breaks, the occurrence of several simple craters with larger floor sizes and lower *PP* scores indicates that the slopes triggered mass wasting in simple craters as well, but on a much smaller scale.

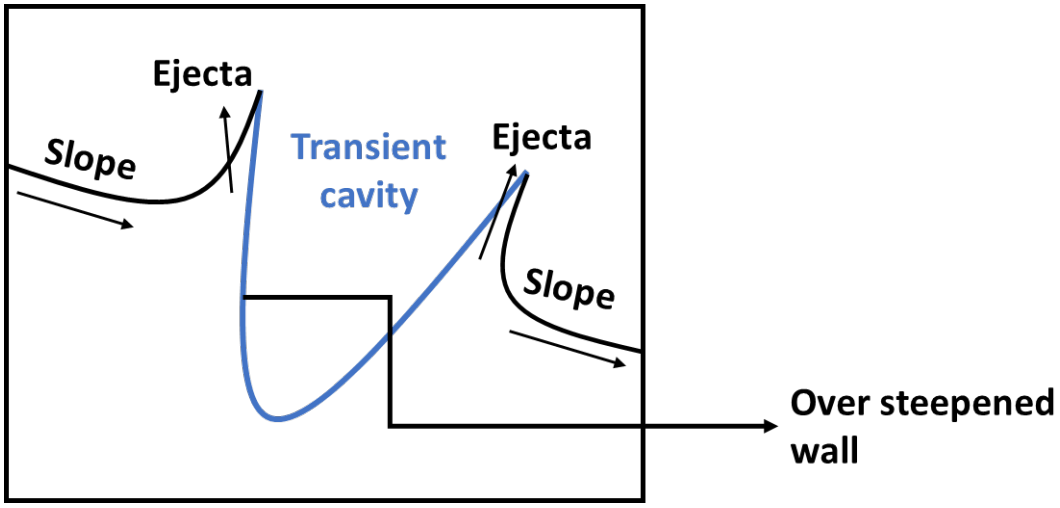

Figure 11. Demonstration of transient cavity formation on a slope. Post excavation stage, the over steepening of cavity wall near the uphill rim sector drives slumping along the wall (Aschauer & Kenkmann, 2017). The ejecta desposited along the slope initiates mass wasting around the downhill rim sector but along the outer cavity wall. Both mass wasting processes may produce deviations from rim circularity.

We encountered four craters with localized slumps that are located on terrains characterized with topographic breaks sloping away from crater walls. Slumping along a wall near the downhill rim sector has lower probability of being as intense as slumping along the uphill sector wall. However, endless impacts on the highlands surface have produced several fractures, fragmented debris and structurally weak zones (Bart et al., 2011; Hartmann, 1973; Heiken et al., 1991; Papike et al., 1982; Soderblom et al., 2015) that, although not visible in the current high resolution image data, could be contributing to subtle heterogeneities in the highlands crust and therefore trigger strength degradation and consequent slumping.

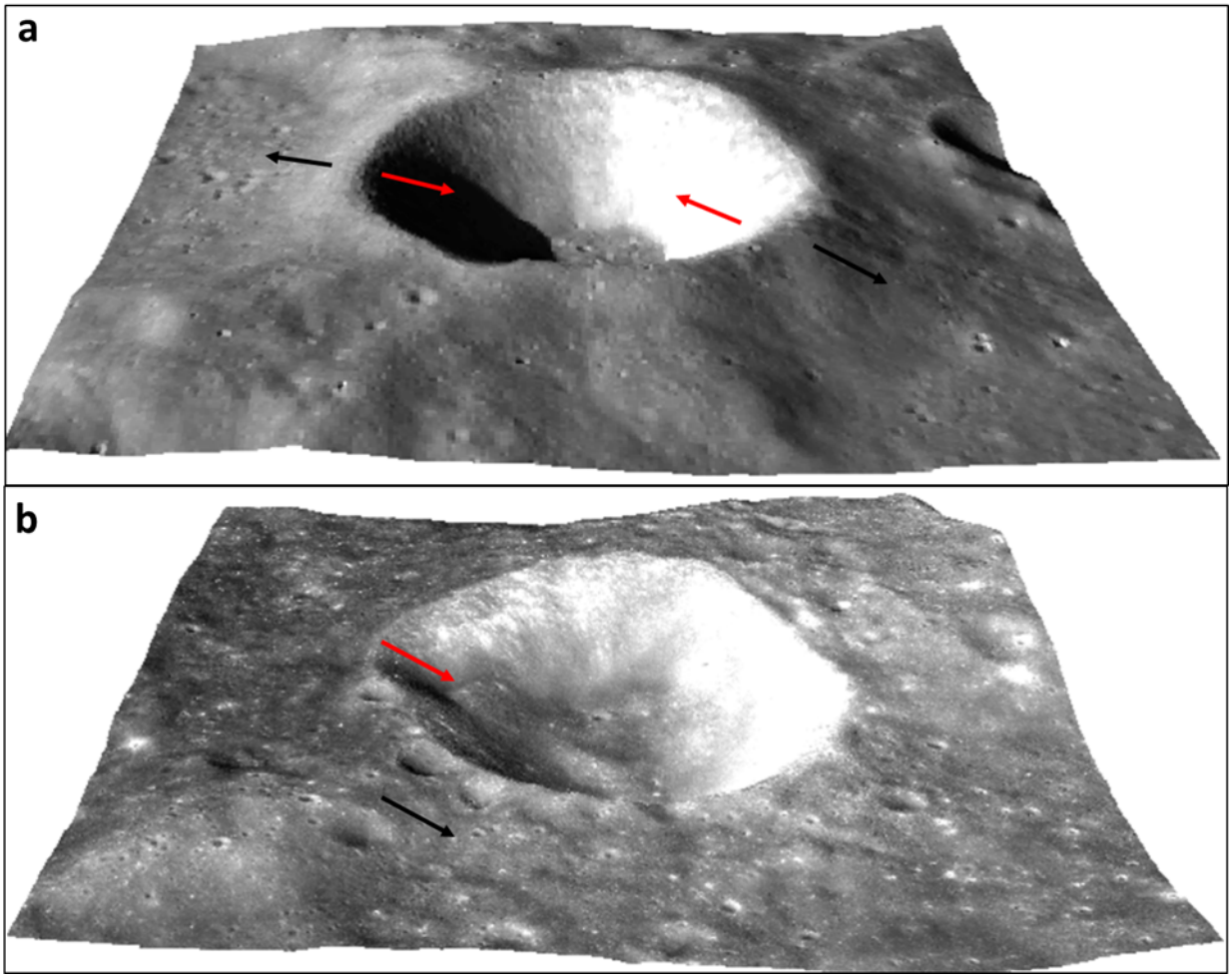

Figure 12. 3D illustrations of crater morphologies on pre-existing slopes. a) 3D WAC view of simple crater Geminus D (30.57°N, 47.29°E) superposing pre-existing crater walls that slope away from Geminus D's walls. B) 3D Kaguya TC view of Crater with localized slumps Unnamed16 (34.92°N, 176.7°E) superposed on a pre-existing crater wall that slopes in the same direction as Unnamed16's walls. The red and black arrows refer to the sloping directions of the craters' walls and the pre-existing topographic breaks, respectively. North is up.

5 Conclusions

For well-preserved ("fresh") lunar craters in the 15-20 km crater diameter range in the lunar highlands that formed on apparently flat or gently undulating terrain, we identified two primary morphologies: simple craters and craters with localized slumps, The morphologies have similar rim-floor depths. The inferred pre-impact topography appeared similar from optical imagery; that is, surfaces

that appeared flat or gradually sloping or consisted of degraded rims and terraces of craters. We performed a detailed geologic and topographic investigation of the craters and their inferred pre-impact terrains using high resolution Kaguya TC images and 512 ppd LOLA DEMs. Our key conclusions are:

[1] Comparison of crater size-frequency distributions between slump and ejecta units suggests that most, if not all, of the observed slumping occurred syn-impact. If and when later slumping occurs it is likely accompanied by other degradational processes that make the crater no longer appear "fresh".

[2] We found no convincing evidence that regional (scales of several tens to hundreds of kilometers) strength variations within the lunar highlands were responsible for whether or not slumping occurred in these similar-sized craters.

[3] Relatively modest slopes in the portions of the target surface can affect crater rim shape, and slopes facing towards crater center can produce modest slumping in what otherwise would be a simple crater.

Acknowledgments

This work was funded by NASA grants NNX14AQ12G and 80NSSC20K0315 to RRH from the Lunar Advanced Science and Exploration Research (LASER) and Lunar Data Analysis (LDAP) programs. The supplemental information contains the size-frequency plots for all of the craters analyzed that are not in Figure 3 (Figure S1) and Tables S1 and S2. For review purposes, the ArcGIS shapefiles used to compile the plots in Figure 3 and Figure S1 have been placed in a Google Drive folder https://drive.google.com/drive/folders/1v-on3PQ_lxNoSrnZnx0W4bgqjRIHdIXW?usp=sharing; upon acceptance the files will be posted to NASA's Scientific and Technical Information (STI) Repository.

References

Arvidson, R., Boyce, J., Chapman, C., Cintala, M., Fulchignoni, M., Moore, H. et al. (1979). Standard techniques for presentation and analysis of crater size-frequency data. *Icarus*, *37*(2), 467-474. doi:https://doi.org/10.1016/0019-1035(79)90009-5.

Aschauer, J., and Kenkmann, T. (2017). Impact cratering on slopes. *Icarus*, *290*, 89-95. doi:https://doi.org/10.1016/j.icarus.2017.02.021.

Bart, G. D., Nickerson, R. D., Lawder, M. T., and Melosh, H. J. (2011). Global survey of lunar regolith depths from LROC images. *Icarus*, *215*(2), 485-490. doi:https://doi.org/10.1016/j.icarus.2011.07.017.

Bouley, S., and Baratoux, D. (2011). *Variation of small crater degradation on the Moon.* Paper presented at 42nd Lunar and Planetary Science Conference, Houston, TX.

Chandnani, M., Herrick, R. R., and Kramer, G. Y. (2019). Geologic Analyses of Causes for Morphological Variations in Lunar Craters within the Sim-

ple-to-Complex Transition. *Journal of Geophysical Research: Planets*, 1238-1265. doi:https://doi.org/10.1029/2018JE005729.

Cintala, M., Wood, C., and Head, J. (1977). *The effects of target characteristics on fresh crater morphology-Preliminary results for the moon and Mercury.* Paper presented at 8th Lunar and Planetary Science Conference Proceedings, Houston, TX.

Cintala, M. J., and Grieve, R. A. (1998). Scaling impact melting and crater dimensions: Implications for the lunar cratering record. *Meteoritics & Planetary Science*, *33*(4), 889-912. doi:https://doi.org/10.1111/j.1945-5100.1998.tb01695.x.

Cooper, H. (1977), A summary of explosion cratering phenomena relevant to meteor impact events In D.J. Roddy et al. (Eds.), *Impact and Explosion Cratering*, pp. 11-44, Pergamon Press, New York.

Cox, E. (1927). A method of assigning numerical and percentage values to the degree of roundness of sand grains. *Journal of Paleontology*, *1*(3), 179-183. doi:http://www.jstor.org/stable/1298056.

Craddock, R. A., and Howard, A. D. (2000). Simulated degradation of lunar impact craters and a new method for age dating farside mare deposits. *Journal of Geophysical Research: Planets*, *105*(E8), 20387-20401. doi:https://doi.org/10.1029/1999JE001099.

Croft, S. K. (1985). The scaling of complex craters. *Journal of Geophysical Research: Solid Earth*, *90*(S02). doi:https://doi.org/10.1029/JB090iS02p0C828.

Dence, A. (1972). *The nature and significance of terrestrial impact structures.* Paper presented at 24th International Geological Congress, Section 15, Montreal, Canada.

Elbeshausen, D., Wünnemann, K., Sierks, H., Vincent, J., and Oklay, N. (2012). *The effect of topography on the impact cratering process on Lutetia.* Paper presented at 43rd Lunar and Planetary Science Conference, Houston, TX.

Fassett, C. I., and Thomson, B. J. (2014). Crater degradation on the lunar maria: Topographic diffusion and the rate of erosion on the Moon. *Journal of Geophysical Research: Planets*, *119*(10), 2255-2271. doi:https://doi.org/10.1002/2014JE004698.

Güldemeister, N., Wünnemann, K., and Poelchau, M. (2015). Scaling impact crater dimensions in cohesive rock by numerical modeling and laboratory experiments. *Geological Society of America Special Papers*, *518*, SPE518-SPE502. doi:https://doi.org/10.1130/2015.2518(02).

Hartmann, W. K. (1973). Ancient lunar mega-regolith and subsurface structure. *Icarus*, *18*(4), 634-636. doi:https://doi.org/10.1016/0019-1035(73)90066-3.

Hartmann, W. K. (1984). Does crater "saturation equilibrium" occur in the solar system? *Icarus*, *60*(1), 56-74. doi:https://doi.org/10.1016/0019-1035

(84)90138-6.

Haruyama, J., Matsunaga, T., Ohtake, M., Morota, T., Honda, C., Yokota, Y. et al. (2008). Global lunar-surface mapping experiment using the Lunar Imager/Spectrometer on SELENE. *Earth, planets and space*, *60*(4), 243-255.

Heiken, G. H., Vaniman, D. T., and French, B. M. (Eds.) (1991). *Lunar sourcebook-A user's guide to the moon*, Cambridge, England; New York: Cambridge University Press.

Howard, K. A. (1974). *Fresh lunar impact craters-Review of variations with size.* Paper presented at 2nd Lunar and Planetary Science Conference Proceedings, Houston, TX.

Kalynn, J., Johnson, C. L., Osinski, G. R., and Barnouin, O. (2013). Topographic characterization of lunar complex craters. *Geophysical Research Letters*, *40*(1), 38-42. doi:https://doi.org/10.1029/2012GL053608

Kenkmann, T., Collins, G. S., and Wünnemann, K. (2012), The modification stage of crater formation, In Gordon R Osinski et al. (Eds.), *Impact cratering: Processes and products*, pp. 60-75, John Wiley & Sons, Oxford, U.K.

Kneissl, T., van Gasselt, S., and Neukum, G. (2010). *New software tool for map-projection-independent crater size-frequency determination in ArcGIS.* Paper presented at 41st Lunar and Planetary Science Conference, Houston, TX.

Kreslavsky, M. A., Head, J. W., Neumann, G. A., Rosenburg, M. A., Aharonson, O., Smith, D. E., and Zuber, M. T. (2013). Lunar topographic roughness maps from Lunar Orbiter Laser Altimeter (LOLA) data: Scale dependence and correlation with geologic features and units. *Icarus*, *226*(1), 52-66. doi:https://doi.org/10.1016/j.icarus.2013.04.027.

Krohn, K., Jaumann, R., Elbeshausen, D., Kneissl, T., Schmedemann, N., Wagner, R. et al. (2014). Asymmetric craters on Vesta: Impact on sloping surfaces. *Planetary and Space Science*, *103*, 36-56. doi:https://doi.org/10.1016/j.pss.2014.04.011.

Krüger, T., Hergarten, S., and Kenkmann, T. (2018). Deriving morphometric parameters and the simple-to-complex transition diameter from a new, high resolution database of fresh lunar impact craters 3 km. *Journal of Geophysical Research: Planets*, *123*(10), 2667-2690. doi:https://doi.org/10.1029/2018JE005545.

Kumar, P. S., Keerthi, V., Kumar, A. S., Mustard, J., Gopala Krishna, B., Ostrach, L. R. et al. (2013). Gullies and landslides on the Moon: Evidence for dry-granular flows. *Journal of Geophysical Research: Planets*, *118*(2), 206-223. doi:https://doi.org/10.1002/jgre.20043.

McKinnon, W. B. (1978). *An investigation into the role of plastic failure in crater modification.* Paper presented at 9th Lunar and Planetary Science Conference Proceedings, Houston, TX.

Melosh, H. J. (1977). *Crater modification by gravity-A mechanical analysis of slumping.* Paper presented at Impact and Explosion Cratering: Planetary and Terrestrial Implications, Flagstaff, AZ.

Melosh, H. J. (1989), Cratering Mechanics: Modification Stage, In *Impact cratering: A geologic process*, pp. 126-161, Oxford University Press, New York.

Melosh, H. J., and Ivanov, B. (1999). Impact crater collapse. *Annual Review of Earth and Planetary Sciences*, *27*(1), 385-415. doi:https://doi.org/10.1146/annurev.earth.27.1.385.

Michael, G. G., and Neukum, G. (2010). Planetary surface dating from crater size–frequency distribution measurements: Partial resurfacing events and statistical age uncertainty. *Earth and Planetary Science Letters*, *294*(3-4), 223-229.

Neukum, G. (1983), Meteoritenbombardement und datierung planetarer oberflächen, Ludwig Maximilianis Univ., Munich, Germany.

Neukum, G., and Ivanov, B. (1994), Crater size distributions and impact probabilities on Earth from lunar, terrestrial-planet, and asteroid cratering data, In T Gehrels et al. (Eds.), *Hazards due to Comets and Asteroids*, pp. 359-416.

Neukum, G., Ivanov, B. A., and Hartmann, W. K. (2001), Cratering records in the inner solar system in relation to the lunar reference system, In *Chronology and evolution of Mars*, pp. 55-86, Springer, doi:https://doi.org/10.1007/978-94-017-1035-0_3.

Neukum, G., König, B., and Arkani-Hamed, J. (1975a). A study of lunar impact crater size-distributions. *The Moon*, *12*(2), 201-229. doi:https://doi.org/10.1007/BF00577878.

Neukum, G., König, B., Fechtig, H., and Storzer, D. (1975b). *Cratering in the Earth-Moon system-Consequences for age determination by crater counting.* Paper presented at 6th Lunar and Planetary Science Conference Proceedings, Houston, TX.

Osinski, G. R., Silber, E. A., Clayton, J., Grieve, R. A., Hansen, K., Johnson, C. L. et al. (2018). Transitional impact craters on the Moon: Insight into the effect of target lithology on the impact cratering process. *Meteoritics & Planetary Science*. doi:https://doi.org/10.1111/maps.13226.

Papike, J. J., Simon, S. B., and Laul, J. C. (1982). The lunar regolith: Chemistry, mineralogy, and petrology. *Reviews of Geophysics*, *20*(4), 761-826. doi:https://doi.org/10.1029/RG020i004p00761.

Pike, R. (1981). *Meteorite craters: Rim height, circularity, and gravity anomalies.* Paper presented at Lunar and Planetary Science Conference.

Pike, R. J. (1974). Depth/diameter relations of fresh lunar craters: Revision from spacecraft data. *Geophysical Research Letters*, *1*(7), 291-294. doi:https://doi.org/10.1029/GL001i007p00291.

Pike, R. J. (1977), Size-dependence in the shape of fresh impact craters on the Moon, In D.J. Roddy et al. (Eds.), *Impact and Explosion Cratering: Planetary and Terrestrial Implications*, pp. 489-509, Pergamon Press, New York.

Pike, R. J. (1980a). *Control of crater morphology by gravity and target type-Mars, Earth, Moon.* Paper presented at 11th Lunar and Planetary Science Conference Proceedings, Houston, TX.

Pike, R. J. (1980b), Geometric interpretation of lunar craters. *USGS Professional Paper,* Rep. 1046-C, C1-C77, Washington: US Govt. Print. Off.

Pike, R. J. (1988), Geomorphology of impact craters on Mercury, In F Vilas et al. (Eds.), *Mercury*, pp. 165-273, University of Arizona Press, Tucson, AZ.

Plescia, J. (2012). Impacts on sloping surfaces: Lunar examples. *Meteoritics and Planetary Science Supplement*, *75*.

Plescia, J. B. (2015), Transitional Crater (Simple/Complex), in *Encyclopedia of Planetary Landforms*, edited, pp. 1-5, Springer, New York, NY, doi:https://doi.org/10.1007/978-1-4614-9213-9_407-2.

Plescia, J. B., Barnouin, O., Anderson, J. L. B., and Cintala, M. J. (2019). *Morphometry and Morphology of Lunar Craters on Slopes.* Paper presented at 50th Lunar and Planetary Science Conference, Houston, TX.

Quaide, W. L., Gault, D. E., and Schmidt, R. A. (1965). Gravitative effects on lunar impact structures. *Annals of the New York Academy of Sciences*, *123*(1), 563-572. doi:https://doi.org/10.1111/j.1749-6632.1965.tb20388.x.

Quaide, W. L., and Oberbeck, V. R. (1968). Thickness determinations of the lunar surface layer from lunar impact craters. *Journal of Geophysical Research*, *73*(16), 5247-5270. doi:https://doi.org/10.1029/JB073i016p05247

Robbins, S. J., and Hynek, B. M. (2012). A new global database of Mars impact craters 1 km: 2. Global crater properties and regional variations of the simple-to-complex transition diameter. *Journal of Geophysical Research: Planets*, *117*(E6). doi:https://doi.org/10.1029/2011JE003967.

Robinson, M., Eliason, E., Hiesinger, H., Jolliff, B., McEwen, A., Malin, M. et al. (2010). *Lunar reconnaissance orbiter camera: first results.* Paper presented at European Planetary Science Congress 2010, Rome, Italy.

Roddy, D. (1977). *Tabular comparisons of the Flynn Creek impact crater, United States, Steinheim impact crater, Germany and Snowball explosion crater, Canada.* Paper presented at Impact and Explosion Cratering: Planetary and Terrestrial Implications, Flagstaff, AZ.

Schultz, P., and Gault, D. (1975). *Seismically induced modification of lunar surface features.* Paper presented at 6th Lunar and Planetary Science Conference Proceedings, Houston, TX.

Senft, L. E., and Stewart, S. T. (2008). Impact crater formation in icy layered terrains on Mars. *Meteoritics & Planetary Science*, *43*(12), 1993-2013. doi:https://doi.org/10.1111/j.1945-5100.2008.tb00657.x

Smith, D. E., Zuber, M. T., Neumann, G. A., Mazarico, E., Head, J., and Torrence, M. H. (2011). *Results from the Lunar Orbiter Laser Altimeter (LOLA): global, high resolution topographic mapping of the Moon.* Paper presented at 42nd Lunar and Planetary Science Conference, Houston, TX.

Smith, E. I., and Hartnell, J. A. (1978). Crater size-shape profiles for the Moon and Mercury: terrain effects and interplanetary comparisons. *The moon and the planets*, *19*(4), 479-511. doi:https://doi.org/10.1007/BF00901976.

Smith, E. I., and Sanchez, A. G. (1973). Fresh lunar craters: Morphology as a function of diameter, a possible criterion for crater origin. *Modern Geology*, *4*, 51-59.

Soderblom, J. M., Evans, A. J., Johnson, B. C., Melosh, H. J., Miljković, K., Phillips, R. J. et al. (2015). The fractured Moon: Production and saturation of porosity in the lunar highlands from impact cratering. *Geophysical Research Letters*, *42*(17), 6939-6944. doi:https://doi.org/10.1002/2015GL065022

Stewart, S. T., and Valiant, G. J. (2006). Martian subsurface properties and crater formation processes inferred from fresh impact crater geometries. *Meteoritics & Planetary Science*, *41*(10), 1509-1537. doi:https://doi.org/10.1111/j.1945-5100.2006.tb00433.x